Upconversion mechanisms in Er^{3+}-doped Ba_2YCl_7

Toni Riedener, Philipp Egger, Jürg Hulliger, and Hans U. Güdel*
Departement für Chemie, Universität Bern, Freiestrasse 3, CH-3000 Bern 9, Switzerland
(Received 31 January 1997)

Efficient near infrared to visible upconversion luminescence is reported in the low phonon-energy host material Ba_2YCl_7:x% Er^{3+} ($x=1$, 10, 100). The upconversion mechanisms upon $^4I_{9/2}$ excitation ($\approx$800 nm) are investigated by means of excitation and time-resolved luminescence spectroscopy. $^2H_{9/2}$ is found to be populated by energy transfer upconversion and excited-state absorption, depending on the excitation energy. Characteristic excited-state absorption peaks in the excitation spectra are used as a fingerprint to determine the population mechanisms for the other states with high luminescence intensities: $^4S_{3/2}/^2H_{11/2}$, $^4F_{9/2}$, and $^4G_{11/2}$. The assignment is confirmed by temperature, concentration, power, and time-dependent measurements. The relative intensities are accounted for by a Judd-Ofelt analysis. [S0163-1829(97)07828-4]

I. INTRODUCTION

Ternary Er^{3+}-doped rare-earth chlorides, bromides, and iodides, such as $RbGd_2X_7$ ($X=$Cl, Br),[1] K_2LaX_5 ($X=$Cl, Br),[2] and $Cs_3Lu_2X_9$ ($X=$Cl, Br, I) (Ref. 3) are known to be efficient infrared to visible upconverters. In contrast to the more extensively investigated oxide and fluoride compounds, a higher number of excited states is available for upconversion and luminescence processes. This is because multiphonon relaxation is strongly suppressed in these heavy halide systems due to their low phonon energies.[4] However, they have a major drawback: they are all very sensitive to moisture and therefore need handling in dry boxes and protection during measurement and storing. To overcome this problem, the alkali ions were exchanged by earth alkali ions. The resulting new materials Ba_2MCl_7 ($M=$Gd–Yb, Y) (Refs. 5 and 6) indeed show a lower sensitivity towards moisture. The compounds used in this study, Ba_2YCl_7 and Ba_2ErCl_7, both crystallize in the monoclinic space group $P2_1/c$. The rare-earth ion is sevenfold coordinated by Cl with a C_1 site symmetry. The nearest-neighbor Er^{3+}-Er^{3+} distance in the structure of Ba_2ErCl_7 is 6.48 Å.[6]

Upconversion of Er^{3+} is known for excitation into all three multiplets in the infrared: $^4I_{13/2}$ ($\approx$1.55 μm), $^4I_{11/2}$ ($\approx$980 nm), and $^4I_{9/2}$ ($\approx$800 nm). In oxide and fluoride compounds, an excitation into $^4I_{9/2}$ is followed by an efficient multiphonon relaxation into the lower-lying $^4I_{11/2}$ due to the relatively high phonon energies. Thus, $^4I_{9/2}$ is not available as a starting level for upconversion.[7,8] In chlorides and bromides, in contrast, the $^4I_{9/2}$-$^4I_{11/2}$ energy gap is too large to be depopulated by multiphonon relaxation, and $^4I_{9/2}$ serves as a starting state for two important upconversion processes. The mechanisms following a $^4I_{9/2}$ excitation in the present low phonon-energy lattices are investigated using excitation and time-resolved luminescence spectroscopy.

II. EXPERIMENT

A. Synthesis

Single crystals of Ba_2YCl_7:x% Er^{3+} ($x=1$, 10, 100) were grown up to a diameter of 10 mm and a length of 20 mm by the Czochralski technique under an inert gas atmosphere. A premelted, off stoichiometric $BaCl_2$:$RECl_3=3:2$ ($RE=Er^{3+}$,Y^{3+}) mixture was used.[5] R_xCl_3 was prepared following the ammonium chloride route described in Refs. 9 and 10.

B. Spectroscopy

All spectra were measured unpolarized with a random crystal orientation. Cooling was done with a closed-cycle cryostat (Air Products) or with a gas-flow technique. The samples were enclosed in a copper cell or sealed into silica ampoules, filled with 600 mbar helium gas for heat dissipation.

Absorption spectra were measured on a Cary 5e (Varian) spectrometer with a typical resolution of 5–10 Å and 1 Å for overview and detailed spectra, respectively.

For near-infrared cw excitation of the crystals a Ti:sapphire laser (Schwartz Electro Optics), pumped by an argon-ion laser in all-lines mode (Spectra Physics 2045-15) with the beam focused on the crystal ($f=60$ mm), was used. Wavelength control for excitation spectra was achieved by an inchworm driven birefringent filter and a wavemeter (Burleigh WA2100). The detection system consisted of a 0.85-m double monochromator (Spex 1402) with gratings blazed at 500 nm (1200 grooves/mm), a cooled photomultiplier tube (RCA 31034), and a photon counting system (Stanford Research SR 400). Power dependences were measured using neutral density filters (Baltzers). Upconversion luminescence spectra were corrected for instrumental response and represent luminescence intensities.

Pulsed excitation for measurement of the dynamics and the lifetimes was achieved by Raman shifting (Quanta Ray RS-1) the output of a Nd:YAG (yttrium aluminum garnet) (Quanta Ray DCR-3, 20 Hz, frequency doubled) pumped dye laser (Lambda Physics FL 3002; Rhodamine 101). The sample luminescence was dispersed by a 0.75-m single monochromator (Spex 1702; blazed at 300 nm, 1200 grooves/mm) with a cooled photomultiplier tube (RCA 31034) and a multichannel scaler (Stanford Research SR430).

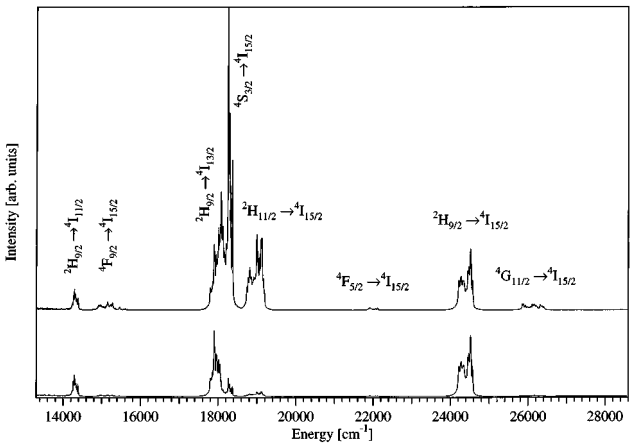

FIG. 1. Upconversion luminescence spectra of Ba_2YCl_7:1% Er^{3+} at room temperature normalized to an equal integrated intensity of the $^2H_{9/2}\rightarrow{}^4I_{15/2}$ transition. Excitation occurred at 12 505 cm^{-1} into a $^4I_{15/2}\rightarrow{}^4I_{9/2}$ ground-state absorption (top) and at 12 115 cm^{-1} into a $^4I_{9/2}\rightarrow{}^2H_{9/2}$ excited-state absorption (bottom) as indicated by the arrows in Fig. 4.

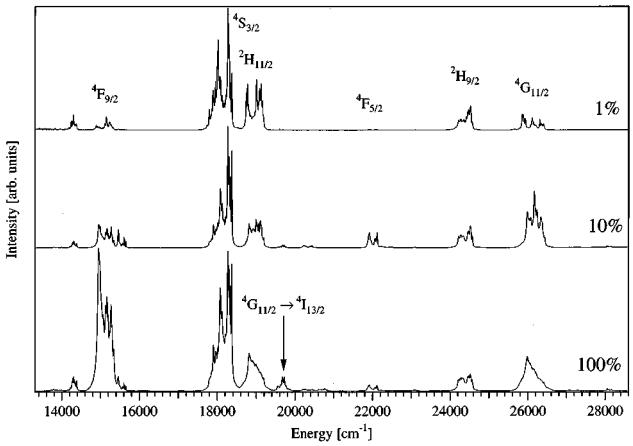

FIG. 2. Er^{3+} concentration dependence of the upconverted luminescence upon excitation at 12 505 cm^{-1}. All spectra are normalized to an equal integrated intensity of the $^2H_{9/2}\rightarrow{}^4I_{15/2}$ transition. To achieve this, the 10% and 100% spectra were scaled down by a factor of 90 and 125, respectively.

III. RESULTS

Figure 1 shows a comparison of upconversion luminescence spectra of Ba_2YCl_7:1% Er^{3+} at room temperature for two different excitation energies. They are scaled to an equal integrated intensity of the $^2H_{9/2}\rightarrow{}^4I_{15/2}$ transition. The upper spectrum was excited at 12 505 cm^{-1} into the $^4I_{15/2}\rightarrow{}^4I_{9/2}$ transition. It is dominated by the green luminescences from $^4S_{3/2}$ and $^2H_{11/2}$ into the ground state $^4I_{15/2}$. The transitions from $^2H_{9/2}$ into the ground state and the first two excited states $^4I_{13/2}$ and $^4I_{11/2}$ are also quite strong. Other luminescence transitions are also indicated in the spectrum, but they are significantly weaker. Upon excitation below the $^4I_{9/2}$ crystal-field levels into a $^4I_{9/2}\rightarrow{}^2H_{9/2}$ excited-state absorption at 12 115 cm^{-1}, the upconversion luminescence spectrum gets simpler (lower trace). The dominating three bands are transitions from $^2H_{9/2}$. All the other transitions account for less than 10% of the intensity.

Upconversion luminescence spectra of Ba_2YCl_7 doped with three different Er^{3+} concentrations are presented in Fig. 2. The spectra were recorded at room temperature and excited into the $^4I_{15/2}\rightarrow{}^4I_{9/2}$ transition around 12 505 cm^{-1}. For a better comparison, the spectra are normalized to a equal integrated intensity of the $^2H_{9/2}\rightarrow{}^4I_{15/2}$ luminescence. With comparable excitation powers, the spectra of the 10% and 100% doped crystals had to be scaled down by factors of 90 and 125, respectively. Besides this overall intensity difference, there is a change in the relative intensities of the transitions. The most pronounced increase of intensity towards higher concentrations is found in the $^4F_{9/2}\rightarrow{}^4I_{15/2}$ transition. In contrast to this, the luminescences from $^4S_{3/2}$ and $^2H_{11/2}$ exhibit the same concentration dependence as the $^2H_{9/2}\rightarrow{}^4I_{15/2}$ transition. An intensity increase from the 1% to the 10% sample is found for the $^4G_{11/2}\rightarrow{}^4I_{15/2}$ transition in the near UV. The shape of this transition is strange in the 100% sample, it has lost its structure and seems to be cut off at higher energies. The $^2H_{11/2}\rightarrow{}^4I_{15/2}$ transition around 19 000 cm^{-1} has a similar shape. The corresponding two absorptions are by far the strongest, see Table I. We therefore attribute the strange shape and the reduced intensity of the luminescence bands to reabsorption processes. This is confirmed by measurements of a Ba_2ErCl_7 powder where these bands are better resolved and more intense. The real intensity of the $^4G_{11/2}\rightarrow{}^4I_{15/2}$ transition is about 10 times higher than in Fig. 2. This can be estimated from the $^4G_{11/2}\rightarrow{}^4I_{13/2}$ transition around 19 700 cm^{-1} which increases by approximately one order of magnitude from the 10% to the pure sample.

Room-temperature excitation spectra in the region of the $^4I_{15/2}\rightarrow{}^4I_{9/2}$ transition for various VIS/UV upconversion luminescences are presented in Fig. 3. The spectra are scaled to the same height of the peak at 12 455 cm^{-1}. At the bottom, Fig. 3 shows absorption spectra of the $^4I_{15/2}\rightarrow{}^4I_{9/2}$ transition, recorded at 15 K and at room temperature. The excitation spectrum for $^4S_{3/2}\rightarrow{}^4I_{15/2}$ detection is very similar to the absorption spectrum at the same temperature.

For $^2H_{9/2}\rightarrow{}^4I_{15/2}$ detection the excitation spectrum re-

TABLE I. Experimental (absorption spectra) and calculated term to term oscillator strengths f ($\times 10^{-6}$) using Eq. (1) with the following parameters: $F^{(2)}=97\,940$ cm^{-1}, $F^{(4)}=69\,850$ cm^{-1}, $F^{(6)}=49\,850$ cm^{-1}, and $\zeta=2366$ cm^{-1} from Ref. 13 and $\Omega_{(2)}=2.529\times10^{-20}$ cm^{-1}, $\Omega_{(4)}=1.424\times10^{-20}$ cm^{-1}, and $\Omega_{(6)}=5.276\times10^{-21}$ cm^{-1} from the fit to the experimental values.

Transition	f_{obs}	f_{calc}	f_{calc}/f_{obs}
$^4I_{15/2}\rightarrow{}^4I_{13/2}$	1292	1 302	1.01
$^4I_{15/2}\rightarrow{}^4I_{11/2}$	383	335	0.87
$^4I_{15/2}\rightarrow{}^4I_{9/2}$	358	331	0.93
$^4I_{15/2}\rightarrow{}^4F_{9/2}$	1721	1 794	1.04
$^4I_{15/2}\rightarrow{}^4S_{3/2}$	378	241	0.64
$^4I_{15/2}\rightarrow{}^2H_{11/2}$	6012	4 658	0.77
$^4I_{15/2}\rightarrow{}^4F_{7/2}$	1286	1 279	0.99
$^4I_{15/2}\rightarrow{}^4F_{5/2}$	281	305	1.08
$^4I_{15/2}\rightarrow{}^4F_{3/2}$	165	186	1.13
$^4I_{15/2}\rightarrow{}^2H_{9/2}$	437	474	1.08
$^4I_{15/2}\rightarrow{}^4G_{11/2}$	9051	10 669	1.18

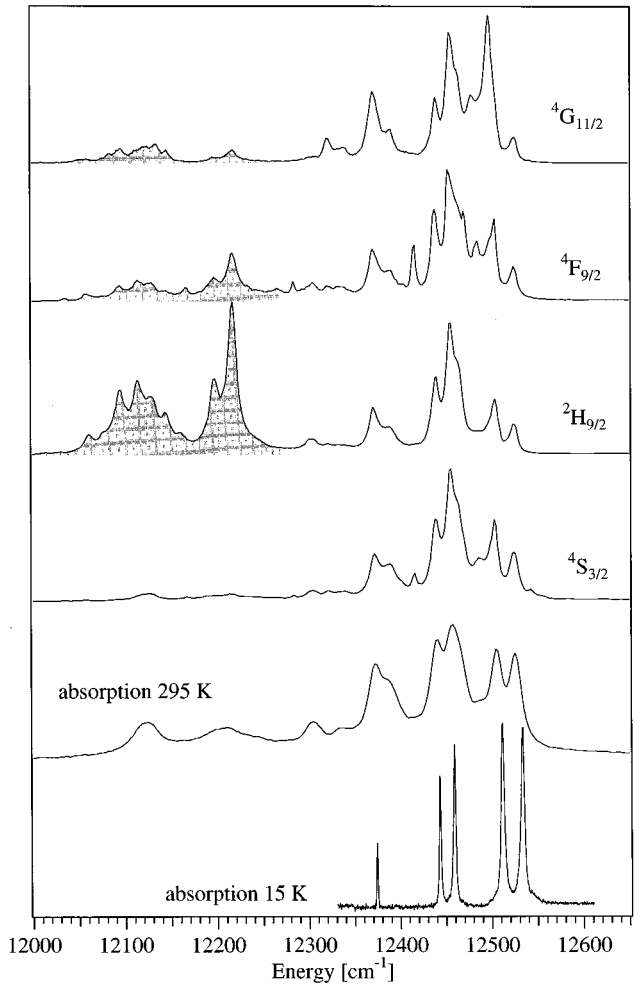

FIG. 3. Room-temperature excitation spectra between 12 000 and 12 650 cm^{-1} of Ba_2YCl_7:1% Er^{3+}, detecting four different upconversion luminescences. The shaded areas indicate the $^4I_{9/2}\rightarrow{}^2H_{9/2}$ excited-state absorptions. The two bottom traces show $^4I_{15/2}\rightarrow{}^4I_{9/2}$ absorption spectra at room temperature and at 15 K.

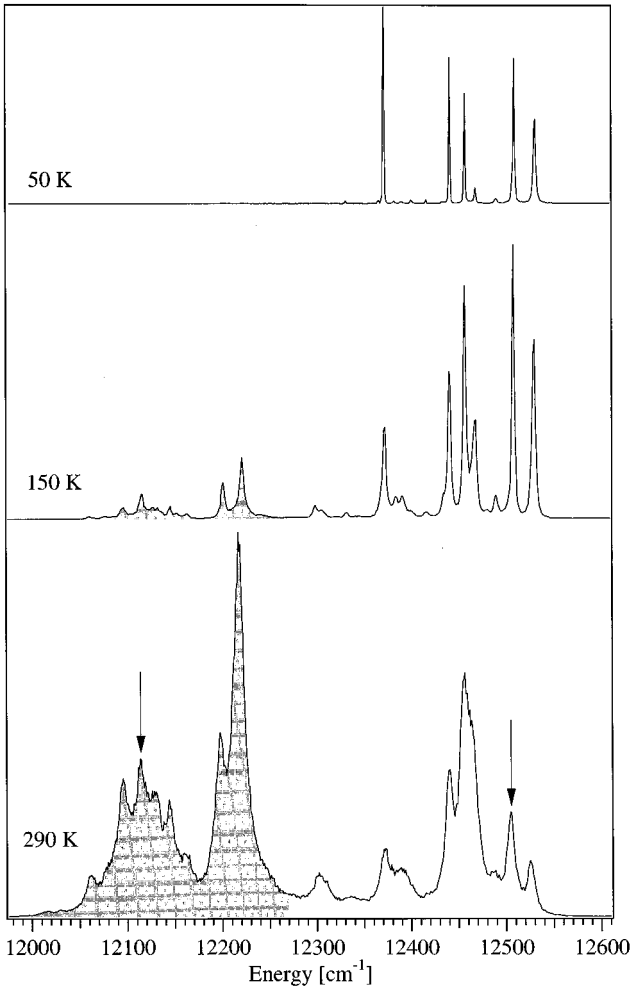

FIG. 4. Temperature dependence of the excitation spectrum, detecting the upconverted $^2H_{9/2}\rightarrow{}^4I_{15/2}$ luminescence of Ba_2YCl_7:1% Er^{3+}. The shaded areas are due to $^4I_{9/2}\rightarrow{}^2H_{9/2}$ ESA processes as in Fig. 3. The arrows indicate the excitation energies used in Figs. 1 and 5.

sembles the absorption spectrum in the high-energy region 12 270–12 550 cm^{-1}, but there is an equally intense band system between 12 020 and 12 270 cm^{-1} which is emphasized by the shaded area in Fig. 3. This band system is also present for $^4F_{9/2}\rightarrow{}^4I_{15/2}$ and $^4G_{11/2}\rightarrow{}^4I_{15/2}$ detection, although less prominent.

Figure 4 shows temperature-dependent excitation spectra of Ba_2YCl_7:1% Er^{3+}, detecting the $^2H_{9/2}\rightarrow{}^4I_{15/2}$ transition at 24 516 cm^{-1}. The spectra were normalized to an equal height of the peak at 12 440 cm^{-1}. The two parts in the spectra already distinguished in Fig. 3 show a distinctly different temperature dependence. Upon cooling, the transitions above 12 270 cm^{-1} (white background) exhibit the normal narrowing expected for f-f transitions. In contrast, the structure below 12 270 cm^{-1} (shaded area) decreases in intensity and vanishes completely below 100 K, a clear indication that they represent a thermally activated process.

We also investigated the concentration dependence of the excitation spectrum for $^2H_{9/2}\rightarrow{}^4I_{15/2}$ detection at room temperature. The low-energy structure below 12 270 cm^{-1}, which is very prominent in the 1% crystal, see bottom trace of Fig. 4, decreases with increasing concentration, and in the pure Ba_2ErCl_7 crystal the excitation spectrum corresponds to the room-temperature absorption spectrum at the bottom of Fig. 3.

In Fig. 5 we report the time evolution after a pulsed excitation (<10 ns) of the upconverted $^2H_{9/2}$ luminescence in Ba_2YCl_7:1% Er^{3+} at room temperature. The insets show the same spectra but in a semilogarithmic plot. Two different excitation energies were used: 12 505 (top) and 12 115 cm^{-1} (bottom), as indicated by the arrows in Fig. 4. The top curve exhibits a rise and a nonexponential decay, whereas the bottom curve has no rise but a clear double exponential decay. The spike at $t=0$ in the upper curve is due to straylight of the exciting laser.

The power dependence of the upconverted luminescence in Ba_2ErCl_7 for different detection wavelengths at room temperature is shown in a double logarithmic plot in Fig. 6. The lines are linear least-square fits through all but the last point. This last point was excluded due to saturation effects at high excitation intensities leading to a leveling off. The fit revealed the following slopes: $^4G_{11/2}$, 2.3 (■); $^4F_{9/2}$, 1.7 (●); $^2H_{9/2}$, 1.6 (○); and $^4S_{3/2}$, 1.6 (□).

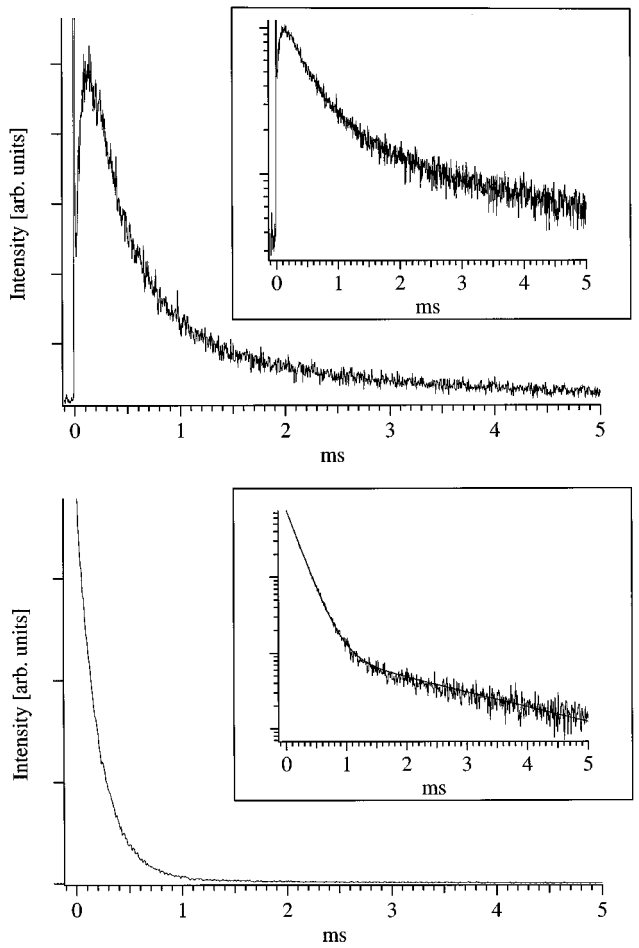

FIG. 5. Temporal behavior of the upconverted $^2H_{9/2}$ luminescence of Ba_2YCl_7:1% Er^{3+} at room temperature after a short (<10 ns) excitation pulse. Excitation energies were 12 505 (top) and 12 115 cm^{-1} (bottom) as indicated by the arrows in Fig. 4. The insets show the same data in semilogarithmic representation. The line in the inset of the bottom figure corresponds to a biexponential fit to the data with the parameters given in Sec. IV B.

IV. DISCUSSION

A. Radiative decay versus multiphonon relaxation

We distinguish three types of deactivation processes of excited states: (i) radiative processes such as luminescences and excited-state absorption, (ii) multiphonon relaxation, and (iii) nonradiative processes based on energy transfer such as upconversion and cross relaxation. It is the competition between these which determines steady-state populations in a cw experiment or excited-state dynamics for pulsed excitation. By chemical and structural variation we influence the relative importance of these processes, which may lead to a completely new competitive situation. In the following, we try to quantify some of the relevant rate constants for the NIR to VIS upconversion processes in Er^{3+}-doped Ba_2YCl_7.

Radiative term to term rate constants can be calculated using the Judd-Ofelt theory.[11,12] The Judd-Ofelt intensity parameters $\Omega_{(\lambda)}$ ($\lambda=2,4,6$) were obtained by fitting the following equation for the oscillator strength of a term to term transition $|SLJ\rangle\rightarrow|S'L'J'\rangle$ within the f-electron configuration to the experimental oscillator strengths derived from room-temperature absorption intensities:

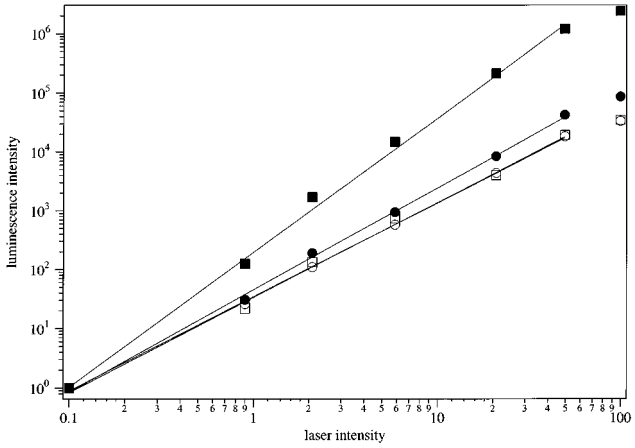

FIG. 6. Power dependence of the upconverted luminescence of Ba_2ErCl_7 at room temperature for different detection wavelengths on a double logarithmic scale: $^4G_{11/2}$, slope 2.3 (■); $^4F_{9/2}$, 1.7 (●); $^2H_{9/2}$, 1.6 (○); and $^4S_{3/2}$, 1.6 (□). For a better comparison of the slopes all the intensities were arbitrarily scaled to a value of 1 for the lowest laser excitation power. The lines are fits through all but the last data point.

$$f=\frac{8\pi mv}{3h}\frac{\chi}{(2J+1)}\sum_{\lambda=2,4,6}\Omega_{(\lambda)}|\langle SLJ\|\mathbf{U}^{(\lambda)}\|S'L'J'\rangle|^2. \tag{1}$$

In Eq. (1), χ is the local-field correction and the last factor is a reduced matrix element of the tensor operator $\mathbf{U}^{(\lambda)}$. All the other symbols have their usual meaning. The reduced matrix elements were expressed in terms of the atomic parameters $F^{(2)}$, $F^{(4)}$, $F^{(6)}$, and ζ, taken from a crystal-field calculation on Er^{3+}-doped $Cs_3Lu_2Cl_9$.[13] The result of this fit as well as the measured oscillator strengths are collected in Table I. The resulting intensity parameters were then used to calculate radiative lifetimes and rate constants of some relevant interexcited-state luminescence transitions. The result is shown in Table II.

The nonradiative multiphonon relaxation rate constant (k_{mp}) is estimated and discussed in terms of the normalized energy-gap law[4]

$$k_{mp}=\beta e^{-\alpha\Delta E/\hbar\omega}. \tag{2}$$

α and β are host-dependent constants, ΔE is the energy gap to the next lower electronic state, and $\hbar\omega$ is the energy of the accepting vibrational mode, with the highest-energy phonons being the most efficient ones. From Raman experiments a highest-energy vibration of $\hbar\omega_{max}=268$ cm^{-1} is derived, in good agreement with other chloride systems.[1–3] According to a rule of thumb multiphonon relaxation becomes dominant when the ratio $\Delta E/\hbar\omega$ gets smaller than 5–6.

We are now in a position to discuss Tables I and II. Considering the approximative nature of the Judd-Ofelt theory, the overall agreement between calculated and measured absorption strengths in Table I is very good. At the bottom of Table II experimental luminescence lifetimes obtained by direct excitation of the respective states are listed and compared with the radiative lifetimes obtained theoretically. The

TABLE II. Calculated radiative term to term rate constants (s^{-1}). Initial states are in the top row. The bottom rows contain calculated radiative and measured room-temperature lifetimes.

	$^4G_{11/2}$	$^2H_{9/2}$	$^4F_{7/2}$	$^2H_{11/2}$	$^4S_{3/2}$	$^4F_{9/2}$	$^4I_{9/2}$
$\rightarrow{}^2H_{9/2}$	2						
$\rightarrow{}^4F_{3/2},{}^4F_{5/2}$	5	0					
$\rightarrow{}^4F_{7/2}$	31	11					
$\rightarrow{}^2H_{11/2},{}^4S_{3/2}$	894	20	1				
$\rightarrow{}^4F_{9/2}$	591	472	22	17	0		
$\rightarrow{}^4I_{9/2}$	208	4832	119	76	56	8	
$\rightarrow{}^4I_{11/2}$	3 416	394	253	433	23	56	2
$\rightarrow{}^4I_{13/2}$	2 213	1107	674	211	305	76	31
$\rightarrow{}^4I_{15/2}$	22 018	1005	2358	4986	711	1463	179
τ_{calc}	34 μs	128 μs	292 μs	175 μs	913 μs	624 μs	4.7 ms
τ_{obs} 1% Er^{3+}		200 μs	9 μs	350 μs			3.3 ms
τ_{obs} 100% Er^{3+}		23 μs	2 μs	7 μs			3.3 ms

measured lifetimes of $^2H_{9/2}$, $^2H_{11/2}/^4S_{3/2}$, and $^4I_{9/2}$ in Ba_2YCl_7:1% Er^{3+} are in good agreement with the values predicted by the Judd-Ofelt theory, but for $^4F_{7/2}$ the experimental value is far too low. This is due to a substantial nonradiative contribution to the experimental decay rate. The energy gap between $^4F_{7/2}$ and $^2H_{11/2}$ is 1241 cm^{-1}. This corresponds to 4.6 phonons of the highest energy. As a consequence, multiphonon relaxation processes are competitive thus reducing the $^4F_{7/2}$ lifetime from 292 to 9 μs. The luminescence lifetimes of the undiluted Ba_2ErCl_7 listed in the bottom row of Table II are, with the exception of $^4I_{9/2}$, substantially reduced from the Ba_2YCl_7:1% Er^{3+} values. This is the result of cross-relaxation processes as well as energy migration to traps.

For the three possible pump states for Er^{3+} in the infrared, $^4I_{13/2}$, $^4I_{11/2}$, and $^4I_{9/2}$, respectively, the energy gap to the next lower state is smallest for $^4I_{9/2}$. In Ba_2ErCl_7 the gap between the lowest crystal-field level of $^4I_{9/2}$ and the highest level of $^4I_{11/2}$ is 2108 cm^{-1}. Thus, in our chloride roughly eight phonons are needed to bridge this gap, leading to a purely radiative $^4I_{9/2}$ lifetime $\tau > 3$ ms even at room temperature. This leads to a high steady-state population of $^4I_{9/2}$ in our excitation scheme, ideal for subsequent upconversion processes. In contrast to this, the $^4I_{9/2} \rightarrow {}^4I_{11/2}$ multiphonon relaxation rate is orders of magnitude higher in fluoride or oxide systems with typical $\hbar\omega_{max} = 350$ cm^{-1} (six phonons) and > 550 cm^{-1} (less than four phonons), respectively. The lifetime of $^4I_{9/2}$ is reduced to 6.6 μs in $LiYF_4$ by predominant multiphonon relaxation into $^4I_{11/2}$, leading to completely different upconversion mechanisms.[8]

B. $^4I_{9/2} \rightarrow {}^2H_{9/2}$: Excited-state absorption versus energy-transfer upconversion

The $^2H_{9/2}$ manifold lies at almost exactly twice the energy of the $^4I_{9/2}$ manifold. Therefore, upconversion into $^2H_{9/2}$ should be possible upon $^4I_{9/2}$ excitation and a spectrum like the one at the bottom of Fig. 1 with a dominant $^2H_{9/2}$ luminescence would be expected. However, the typical upconversion luminescence spectrum upon excitation into a crystal-field level of $^4I_{9/2}$, as depicted in the upper part of Fig. 1, shows a number of additional luminescences. The dominant features are due to $^2H_{11/2}/^4S_{3/2} \rightarrow {}^4I_{15/2}$ transitions. At higher Er^{3+} concentrations the $^4F_{9/2} \rightarrow {}^4I_{15/2}$ and $^4G_{11/2} \rightarrow {}^4I_{15/2}$ also gain intensity (Fig. 2). Obviously, the simple picture of just one upconversion process does not hold in these systems. Additional mechanisms populating all these states have to be considered and will be discussed in Secs. IV C–IV E. In the present section we concentrate on the mechanisms for $^2H_{9/2}$ population.

There are three basically different mechanisms to reach $^2H_{9/2}$ from $^4I_{9/2}$: upconversion by radiationless energy transfer (ETU), excited state absorption (ESA), and avalanche upconversion. In our system, avalanche upconversion can be excluded, because none of the typical signatures for an avalanche process could be found.[14–17]

The two other mechanisms are schematically represented in the upper part of Fig. 7. The ETU on the left is a two-ion process. The energy of an ion in an intermediate state is transferred nonradiatively onto another ion thereby exciting it into a higher excited state. The ESA upconversion on the right consists of two consecutive excitation steps on a single ion.

Excitation spectra detecting the upconverted $^2H_{9/2} \rightarrow {}^4I_{15/2}$ luminescence provide a first possibility to distinguish between these two mechanisms. In the case of an energy-transfer upconversion, the $^4I_{9/2}$ multiplet acts as a sensitizer for both ions and therefore an excitation spectrum similar to an $^4I_{15/2} \rightarrow {}^4I_{9/2}$ absorption spectrum is expected. The room-temperature excitation spectrum for $^2H_{9/2} \rightarrow {}^4I_{15/2}$ detection in Fig. 3 is indeed very similar to the corresponding absorption spectrum above 12 270 cm^{-1}. However, below 12 270 cm^{-1} there are additional intense peaks. For an ESA process we would expect such additional peaks corresponding to the second step, i.e., the $^4I_{9/2} \rightarrow {}^2H_{9/2}$ transition. From high-resolution absorption spectra it is known that this second step is lower in energy than the $^4I_{9/2}$ crystal-field excitations.

Table III provides the experimental evidence that the additional peaks between 12 020 and 12 270 cm^{-1} are indeed due to this $^4I_{9/2} \rightarrow {}^2H_{9/2}$ ESA process. They occur exactly at the energies expected on the basis of the high-resolution absorption spectra.

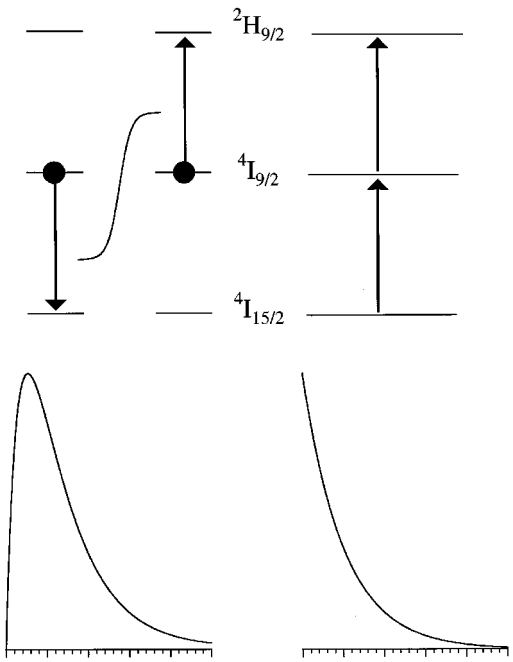

FIG. 7. Schematic representation of the two principal upconversion mechanisms to populate $^2H_{9/2}$ by NIR excitation around 800 nm. Upconversion energy transfer (left) and excited-state absorption (right). The corresponding expected time dependence of the $^2H_{9/2}$ population after a pulsed excitation is schematically shown below.

Because $^4I_{9/2} \rightarrow {}^2H_{9/2}$ ESA is lower in energy, the first step $^4I_{15/2} \rightarrow {}^4I_{9/2}$ has to be thermally activated. Absorption from higher crystal-field levels of $^4I_{15/2}$ into $^4I_{9/2}$ below 12 270 cm^{-1} is indeed possible as shown in the room-temperature absorption spectrum of Fig. 3. As the mechanism depends on this thermal activation, the ESA upconversion disappears at lower temperatures, see Fig. 4.

Time-dependent measurements following a pulsed excitation are another possibility to distinguish between ETU and ESA upconversion processes.[18] ESA upconversion has to take place during the excitation pulse, whereas the ETU process can proceed after the $^4I_{9/2}$ excitation by the laser pulse. The transients for the two processes are schematically depicted in Fig. 7. The measured room-temperature transients of the upconverted $^2H_{9/2} \rightarrow {}^4I_{15/2}$ luminescence are shown in Fig. 5 with semilogarithmic plots in the insets. They clearly show the expected signatures. Excitation at 12 505 cm^{-1} (upper trace) essentially leads to an ETU process, whereas 12 115-cm^{-1} excitation (lower trace) leads to an ESA process. The semilogarithmic plot of the lower trace clearly shows a biexponential decay behavior. A fit reveals a 98.5% component with $\tau = 200\ \mu s$ and a 1.5% component with $\tau = 2.5$ ms. From a comparison with the bottom of Table II we recognize the $\tau = 200\ \mu s$ as the $^2H_{9/2}$ lifetime. Since it accounts for 98.5% of the total intensity we are observing an almost pure ESA upconversion luminescence excited as shown on the top right of Fig. 7. The minority ($<2\%$) with $\tau = 2.5$ ms is close to the $^4I_{9/2}$ lifetime. We are obviously observing a very small fraction of ETU upconversion also for this excitation. Conversely, the upper trace in Fig. 5, which is dominantly due to ETU, is slightly contaminated by an ESA process. This follows from the fact that there is some initial population at time $t = 0$. It is thus not possible to extract meaningful numbers from the transient curve with the exception of the long tail that corresponds to the $^4I_{9/2}$ lifetime. $^4I_{9/2}$ acts as a long-lived reservoir of excitation and thus determines the decay at long times.

TABLE III. Comparison of calculated $^4I_{9/2} \rightarrow {}^2H_{9/2}$ ESA energies (E_{calc}), derived from the high resolution, 15-K absorption spectra, and measured ESA energies (E_{obs}) from Figs. 3 and 4.

Transition	E_{calc}	E_{obs}	ΔE
$^4I_{9/2}(0) \rightarrow {}^2H_{9/2}(0')$	12 100		
$^4I_{9/2}(0) \rightarrow {}^2H_{9/2}(1')$	12 146	12 146	0
$^4I_{9/2}(0) \rightarrow {}^2H_{9/2}(2')$	12 164	12 164	0
$^4I_{9/2}(0) \rightarrow {}^2H_{9/2}(3')$	12 202	12 201	−1
$^4I_{9/2}(0) \rightarrow {}^2H_{9/2}(4')$	12 223	12 222	−1
$^4I_{9/2}(1) \rightarrow {}^2H_{9/2}(0')$	12 031		
$^4I_{9/2}(1) \rightarrow {}^2H_{9/2}(1')$	12 077		
$^4I_{9/2}(1) \rightarrow {}^2H_{9/2}(2')$	12 095	12 096	+1
$^4I_{9/2}(1) \rightarrow {}^2H_{9/2}(3')$	12 133	12 132	−1
$^4I_{9/2}(1) \rightarrow {}^2H_{9/2}(4')$	12 154	12 154	0

The different upconversion mechanisms in the 1% sample can already be seen visually. Excitation above 12 270 cm^{-1} into the crystal-field levels of $^4I_{9/2}$ leads to a typical green luminescence, whereas excitation into the $^4I_{9/2} \rightarrow {}^2H_{9/2}$ ESA leads to a bluish-white luminescence. As shown in Fig. 1, the ESA excitation results in an almost pure $^2H_{9/2}$ luminescence. This means that there are no competitive processes deactivating $^2H_{9/2}$.

The observed concentration dependence of the relative importance of the two upconversion processes in Fig. 2 is intuitively understandable. In the 1% sample the average Er^{3+}-Er^{3+} distance is too large for substantial ETU to take place. In the undiluted sample, on the other hand, the closest Er^{3+}-Er^{3+} contact is 6.48 Å, sufficient by far for nonradiative energy transfer. ETU is thus the dominant mechanism in Ba_2ErCl_7.

C. Mechanism for the $^4S_{3/2}$ population

Excitation into $^4I_{9/2}$ leads to a substantial $^2H_{11/2}/{}^4S_{3/2}$ upconversion luminescence at room temperature, see Figs. 1 and 2. With the evidence presented in Figs. 1–6 and with the arguments developed in Sec. IV B we are now in a position to identify the mechanism by which $^4S_{3/2}$ is populated. At room temperature there is always a concomitant $^2H_{11/2}$ population because the two states are close in energy.

We note the following characteristic features of the $^4S_{3/2}$ luminescence: the concentration and power dependence is the same as for $^2H_{9/2}$ luminescence (Figs. 2 and 6); the excitation spectrum corresponds to the $^4I_{15/2} \rightarrow {}^4I_{9/2}$ absorption spectrum, i.e., there are no extra lines below 12 270 cm^{-1} (Fig. 3).

Population of $^4S_{3/2}$ by any process through a $^2H_{9/2}$ intermediate can be ruled out because in Sec. IV B it was found that the $^2H_{9/2}$ depopulation occurs predominantly by luminescence. This is supported by the absence of any lines below 12 270 cm^{-1} in the excitation spectrum detecting $^4S_{3/2}$. This is an important conclusion because it is very

restrictive. In particular, we can rule out multiphonon relaxation from $^2H_{9/2}$, as we would have expected from the energy gaps. The only plausible mechanism to populate $^4S_{3/2}$ is the ETU upconversion mechanism shown with full arrows in Fig. 8. The energy differences between the multiplets $\Delta E(^4S_{3/2}$-$^4I_{9/2})$ and $\Delta E(^4I_{9/2}$-$^4I_{13/2})$ are almost equal, with the latter larger by 102 cm^{-1} when only the lowest crystal-field level of $^4I_{9/2}$ is populated. Phonon-assisted ETU upconversion processes $^4I_{9/2}+{}^4I_{9/2}\rightarrow{}^4S_{3/2}+{}^4I_{13/2}$ are thus possible down to the lowest temperatures as observed experimentally. The situation is completely analogous to the ETU upconversion process $^4I_{9/2}+{}^4I_{9/2}\rightarrow{}^2H_{9/2}+{}^4I_{15/2}$ shown by empty arrows in Fig. 8 and discussed in the previous section. The two ETU upconversion processes represented by full and empty arrows in Fig. 8 compete in the deactivation of the high $^4I_{9/2}$ population. That is why the corresponding luminescences have the same concentration and power dependence.

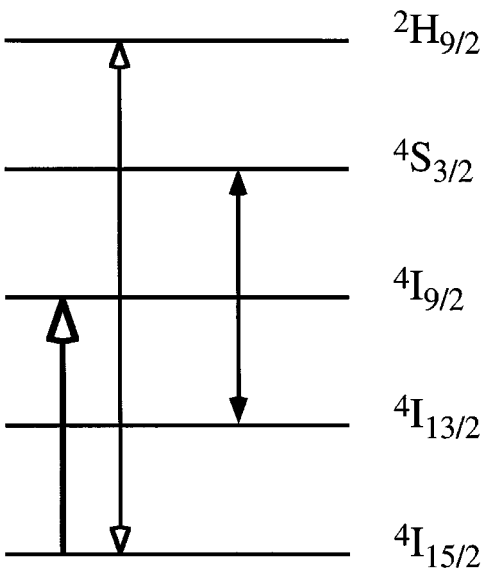

FIG. 8. Schematic representation of the most probable $^4S_{3/2}$ population mechanism (full arrows) after $^4I_{9/2}$ laser excitation (open arrow). The $^2H_{9/2}$ population mechanism (open arrows) is included for comparison.

D. Mechanisms to populate $^4F_{9/2}$

A characteristic for the $^4F_{9/2}$ upconversion luminescence is its much stronger concentration dependence than $^2H_{9/2}$, see Fig. 2. Concentration dependence is typical for energy-transfer processes. With the excitation energy used in Fig. 2, the $^2H_{9/2}$ population itself originates from an energy-transfer process. Thus, the even stronger concentration dependence of the $^4F_{9/2}$ upconversion luminescence indicates two or more successive energy-transfer processes. A three center process is excluded because the $^4F_{9/2}$ luminescence is observed even at the low concentration of 1%. The power dependence of the $^4F_{9/2}$ upconversion luminescence is 1.7 (Fig. 6) and thus only slightly higher than that of $^2H_{9/2}$ or $^4S_{3/2}$. We conclude that it arises by a two-photon process. The excitation spectrum in Fig. 3 is again similar to the absorption spectrum in the region above 12 270 cm^{-1}. But there are also peaks below 12 270 cm^{-1} in the region of the $^4I_{9/2}\rightarrow{}^2H_{9/2}$ ESA. These are similar to the excitation spectrum for $^2H_{9/2}$, but significantly less intense.

In Fig. 9 we show by full arrows two possible energy-transfer mechanisms (a) and (b) for the population of $^4F_{9/2}$. They are both energetically favorable, in that the downward arrows are slightly longer than the upward arrows. In a phonon-assisted mechanism they can thus both persist down to the lowest temperatures. This is in agreement with the observation of $^4F_{9/2}$ upconversion luminescence in the 100% crystal down to 10 K. The basis of Fig. 9 was established in Secs. IV B and IV C: High populations in the excited states $^4I_{9/2}$ (laser excitation) as well as $^2H_{9/2}$, $^4S_{3/2}$, and $^4I_{13/2}$ (all by upconversion, see open arrows in Fig. 9). Both mechanisms (a) and (b) are particularly efficient in producing $^4F_{9/2}$ population, because both partners in the cross-relaxation process end up in $^4F_{9/2}$.

Based on the experimental evidence presented above we identify mechanism (a) as important. At least part of the $^4F_{9/2}$ population occurs via the $^2H_{9/2}$ intermediate, because we have the $^4I_{9/2}\rightarrow{}^2H_{9/2}$ ESA signature in the excitation spectrum. These lines are not as prominent as for $^2H_{9/2}$ detection, but this would be expected even if (a) was the only relevant mechanism, because only one of the partners in the process (a) carries the ESA signature. We cannot rule out nor prove a participation of process (b).

E. Mechanisms to populate $^4G_{11/2}$

The $^4G_{11/2}$ upconversion luminescence in the near UV which is quite prominent in the present system can only occur in low phonon-energy hosts. The energy gap to the next lower $^2H_{9/2}$ manifold is around 1600 cm^{-1}, which is quickly depopulated in oxides and fluorides. Since the $^4I_{15/2}\leftrightarrow{}^4G_{11/2}$ transition has one of the highest oscillator strengths, the intense $^4G_{11/2}$ luminescence observed here is

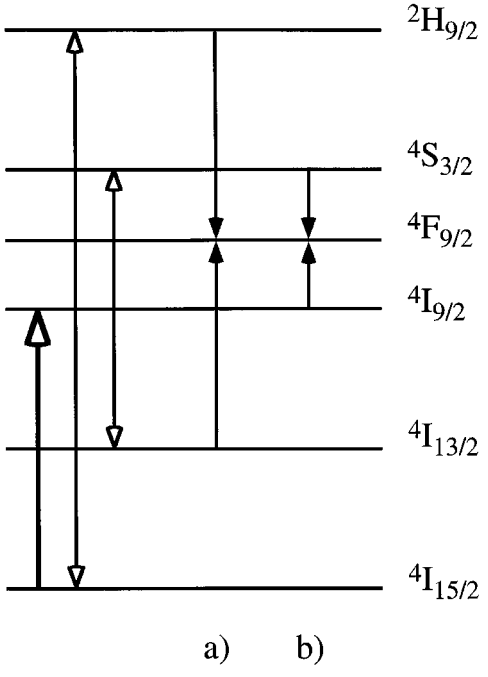

FIG. 9. As in Fig. 8, with additional mechanisms (a) and (b) to populate $^4F_{9/2}$ (full arrows).

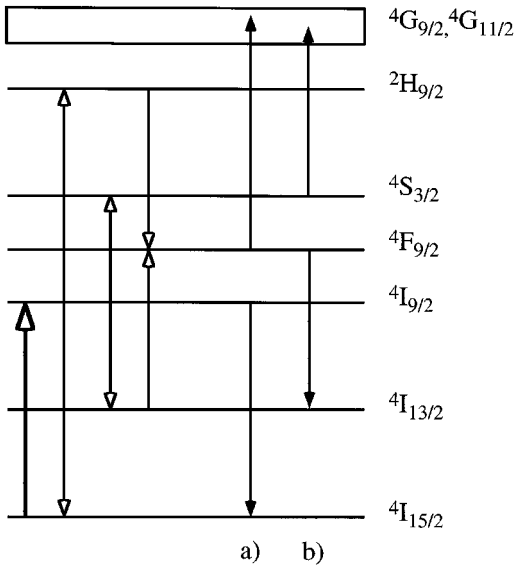

FIG. 10. As in Fig. 9, with additional mechanisms (a) and (b) to populate $^4G_{11/2}$ (full arrows). A number of mechanisms starting at $^2H_{9/2}$ are not included.

important for an evaluation of the potential of induced emission processes. We are, therefore, interested in exploring the possible population mechanisms of $^4G_{11/2}$.

Similar to the $^4F_{9/2}$ luminescence, the $^4G_{11/2}$ luminescence shows a very strong concentration dependence (Fig. 2), indicating at least two successive energy-transfer processes. The luminescence intensity in the pure sample is reduced to about 10% by reabsorption. As $^4G_{11/2}$ lies considerably higher than twice the energy of the $^4I_{9/2}$ pump level, at least three photons are needed to reach it. This is reflected in the power dependence (Fig. 6) with a slope of 2.3, clearly steeper than the 1.6–1.7 of the other levels.

Using the same reasoning as in the previous sections, we consider possible mechanisms for the population of $^2H_{9/2}$. The energy difference between $^4G_{11/2}$ and the next higher state $^4G_{9/2}$ is only 775 cm^{-1} and therefore an excitation into $^4G_{9/2}$ decays immediately by multiphonon relaxation into $^4G_{11/2}$. This enlarges the energy range, and in Fig. 10 the two states are connected. Initial states for possible upconversion or cross-relaxation processes are the same as in the previous section plus $^4F_{9/2}$. The two mechanisms (a) and (b) in Fig. 10 are energetically favorable. Both are upconversion mechanisms. No reasonable cross relaxation is found, since there are no populated high-energy states available.

A number of mechanisms involving at least one ion in $^2H_{9/2}$ would be energetically favorable, but they have not been included in Fig. 10. The reason lies in the low relative intensity of the $^4I_{9/2} \rightarrow {}^2H_{9/2}$ ESA lines below 12 270 cm^{-1} in the excitation spectrum of the $^4G_{11/2}$ upconversion luminescence, see Fig. 3. We cannot discriminate between the processes (a) and (b) on the basis of our experimental data. (a) appears more likely because it involves $^4I_{9/2}$ which, being directly populated by the laser, should have the highest excited-state population.

V. CONCLUSIONS

We have developed fingerprinting techniques to distinguish between upconversion by energy transfer and by excited-state absorption in the title compounds. Furthermore, we have been able to establish the major population mechanisms of the states with the most intense luminescences upon excitation into $^4I_{9/2}$.

By only a small variation of the excitation energy, $^2H_{9/2}$ can be almost exclusively populated by an ESA or an ETU process. Excitation spectra allow an easy discrimination between the two main mechanisms, but the temporal behavior after a pulsed excitation is needed to recognize the slight contribution of the other mechanism. The ESA mechanism is very selective and leads to a simple luminescence spectrum, consisting essentially of transitions from $^2H_{9/2}$. The highest ESA upconversion efficiencies are achieved when the excitation is tuned to the second absorption step, i.e., the actual $^4I_{9/2} \rightarrow {}^2H_{9/2}$ ESA. There is a nonzero ground-state absorption at these energies due to thermally populated crystal-field levels in the ground state. The first step, is thus rather inefficient because it is not tuned to a $^4I_{15/2} \rightarrow {}^4I_{9/2}$ energy difference. The efficiency of this ESA upconversion could therefore be greatly enhanced by a two-color excitation in which the two laser lines are tuned to the first and second excitation step, respectively. We have recently performed such experiments on the related $LaCl_3$:Er^{3+} system and achieved enhancements of the excitation efficiency of at least two orders of magnitude. Since $^2H_{9/2}$ essentially decays by radiative processes, this gain in excitation efficiency shows as a gain in the spontaneous emission intensity. However, ESA is only competitive at low Er^{3+} concentrations. With increasing Er^{3+} concentrations the average Er^{3+}-Er^{3+} distance gets smaller and thus enhances the energy-transfer upconversion probability. The ESA peaks in the excitation spectra serve as a characteristic signature for $^2H_{9/2}$. Their presence or absence indicates whether $^2H_{9/2}$ is involved in a population mechanism or not.

The system Ba_2YCl_7:Er^{3+} has a high upconversion efficiency.[5] We are presently exploring the possibilities of stimulated emission and possibly laser action in Er^{3+}-doped Ba_2YCl_7.

ACKNOWLEDGMENTS

We thank M. P. Hehlen for providing his Judd-Ofelt program. Financial support by the Swiss National Science Foundation and by a grant from the priority program ''Optics'' is gratefully acknowledged.

*Author to whom correspondence should be addressed.

[1] T. Riedener, K. Krämer, and H. U. Güdel, Inorg. Chem. **34**, 2745 (1995).

[2] K. Krämer and H. U. Güdel, J. Alloys Compd. **207/208**, 128 (1994).

[3] M. P. Hehlen, K. Krämer, H. U. Güdel, R. A. McFarlane, and R. N. Schwartz, Phys. Rev. B **49**, 12 475 (1994).

[4] L. A. Riseberg and H. W. Moos, Phys. Rev. **174**, 429 (1968).

[5] P. Egger, P. Rogin, T. Riedener, H. U. Güdel, M. S. Wickleder, and J. Hulliger, Adv. Mater. **8**, 668 (1996).

[6] M. S. Wickleder, P. Egger, T. Riedener, N. Furer, H. U. Güdel, and J. Hulliger, Chem. Mater. **8**, 2828 (1996).
[7] W. Lenth and R. M. Macfarlane, J. Lumin. **45**, 346 (1990).
[8] M. Pollnau, Th. Graf, J. E. Balmer, W. Lüthy, and H. P. Weber, Phys. Rev. A **49**, 3990 (1994).
[9] J. B. Reed, B. S. Hopkins, and L. F. Audrieth, Inorg. Synth. **1**, 28 (1936).
[10] G. Meyer, Inorg. Synth. **22**, 1 (1983).
[11] B. R. Judd, Phys. Rev. **127**, 750 (1962).
[12] G. S. Ofelt, J. Chem. Phys. **37**, 511 (1962).
[13] S. R. Lüthi, H. U. Güdel, M. P. Hehlen, and J. R. Quagliano (unpublished).
[14] U. Oetliker, M. J. Riley, P. S. May, and H. U. Güdel, J. Lumin. **53**, 553 (1992).
[15] J. S. Chivian, W. E. Case, and D. D. Eden, Appl. Phys. Lett. **35**, 124 (1979).
[16] M. E. Koch, A. W. Kueny, and W. E. Case, Appl. Phys. Lett. **56**, 1083 (1990).
[17] T. Herbert, R. Wannemacher, R. M. Macfarlane, and W. Lenth, Appl. Phys. Lett. **60**, 2592 (1992).
[18] M. P. Hehlen, G. Frei, and H. U. Güdel, Phys. Rev. B **50**, 16 246 (1994).